Why Little Red Dots Disappear at z < 3: Evolution of Number Density and Halo Mass

Chenxuan Zhang[1], Huanian Zhang[1,*], Qingwen Wu[1,*], Luis C. Ho[2,3], and Jian-Min Wang[4,5,6]

[1]Department of Astronomy, School of Physics, Huazhong University of Science and Technology, Wuhan, Hubei 430074, China
[2]Kavli Institute for Astronomy and Astrophysics, Peking University, Yiheyuan Road, Beijing, 100871, Beijing, China
[3]Department of Astronomy, School of Physics, Peking University, Yiheyuan Road, Beijing, 100871, Beijing, China
[4]Key Laboratory for Particle Astrophysics, Institute of High Energy Physics, Chinese Academy of Sciences, Yuquan Road, Beijing, 100049, Beijing, China
[5]National Astronomical Observatories of China, Chinese Academy of Sciences, Datun Road, Beijing, 100101, Beijing, China
[6]School of Astronomy and Space Science, University of Chinese Academy of Sciences, Yuquan Road, Beijing, 100049, Beijing, China

A significant puzzle in extragalactic astronomy is the scarcity of Little Red Dots (LRDs) at $z < 3$, compared to their higher abundance at earlier epochs. To understand this transition, we investigate the cosmic evolution of LRD environments. We measure the overdensity for LRDs and the general galaxy population at $3 < z < 7$, and find that at $z > 4$, LRDs predominantly reside in under-dense regions relative to the general galaxy population. By $z \sim 3.5$, however, this environmental contrast roughly diminishes, and LRDs are found in regions of comparable density to typical galaxies. Simultaneously, the dark matter halo masses of LRDs, inferred from large-scale clustering, grow rapidly from $\lesssim 10^{10.1}\,M_\odot$ at $z \sim 7.5$ to $\sim 10^{11.3}\,M_\odot$ at $z \sim 3.5$, where the halo mass becomes close to that of normal galaxies at lower redshift. Applying an empirical stellar-to-halo mass scaling relation, we derive stellar masses for LRDs; these show that black hole masses remain over-massive relative to stellar mass at $z > 4$, but converge toward the local $M_* - M_{\rm BH}$ scaling relation by $z \sim 3.5$. The coherent evolution of LRDs' large-scale environments – as expressed by their overdensity and halo mass – points to a distinct evolutionary pathway from that of normal galaxies. The significantly increased halo masses of LRDs lead to larger galaxy sizes, driven primarily by the potential enhancement of halo spins. Consequently, these sources are no longer as compact as typical high-redshift LRDs. Meanwhile, the depletion of dense gas and/or elevated star formation in their host galaxies would also significantly alter the spectral energy distribution of LRDs.

The *James Webb Space Telescope* (JWST) has uncovered a previously unrecognized population of compact, red, high-redshift sources, commonly referred to as Little Red Dots (LRDs), distinguished by their unusually steep red rest-frame optical continua, compact size with $\lesssim$ a few $\times 100$ pc, and often unresolved morphologies in NIRCam imaging[1–5]. Spectroscopic observations reveal that many LRDs exhibit broad Balmer emission lines, with full widths at half maximum exceeding ~ 1000 km s^{-1}, indicative of a central supermassive black hole (SMBH) with inferred mass of order $\sim 10^6 - 10^8\,M_\odot$[4–7]. The V-shaped spectral energy distributions (SEDs) are the most distinctive features of LRDs in the rest-frame UV-to-optical bands, which transit near the Balmer limit[2,8,9]. The absorption features on some broad Balmer lines[10], and the absence of X-ray detections[11,12], are sometimes attributed to the possible absorption by the dense gas surrounding central SMBHs[13–15]. The V-shaped SEDs are frequently explained by the co-existence of AGNs and galaxies with strong dust extinction[16–18]. However, the lack of direct detections of strong dust emission for high-redshift LRDs appears to be in tension with this interpretation[19,20].

The intrinsically red accretion disk model[21–23] and an envelop dense gas model have been proposed as alternative explanations[13–15].

The SMBH masses of LRDs, estimated using single-epoch virial methods, are orders of magnitude higher relative to their host galaxy masses than those observed in the local Universe[3,24–27]. It should be noted that robust measurements of both SMBH mass and host galaxy stellar mass remain challenging for LRDs, owing to their peculiar observational properties. For example, it is still not fully clear that the profile of broad lines in LRDs is caused by virial motion or electron scattering in a dense ionized gas[28,29]. Furthermore, no strong extended stellar component has been resolved in these LRDs to date, and the radiation from optical to UV waveband is also controversial (e.g., radiation from either galaxy, AGN disk, or photosphere surrounding a SMBH[9,21,30,31]). Therefore, precise measurements of both the stellar masses and SMBH masses of LRDs are crucial for understanding the co-evolution of SMBHs and their host galaxies in the early Universe. Despite being individually faint, LRDs are surprisingly abundant at $z > 4$, with cosmic number densities of $\Phi \sim 10^{-5} - 10^{-4}$ cMpc^{-3} (comoving Mpc)[5,6,24,32], significantly exceeding the space densities of comparably luminous UV-bright quasars at similar epochs[33–40]. The presence of over-massive SMBHs in LRDs implies that either the SMBH growth or the host galaxy assembly proceeds differently from that in other galaxies or quasars. The environment has long been recognized as an important factor influencing the evolution of galaxies and SMBHs. In a recent study, it was found that LRDs may preferentially reside in under-dense regions compared to typical galaxies, based on a sample of photometrically selected LRDs[41]. Thereby, systematic investigations of large-scale environments for a large sample of spectroscopically confirmed LRDs have the potential to shed new light on their distinctive properties and on the disappearance of LRDs at $z < 3$[24,42,43].

In this work, we explore the large-scale environments and halo masses of LRDs based on 98 spectroscopically confirmed LRDs[7,44,45] at $3 < z < 7$ identified in JWST/NIRCam and NIRSpec observations across six deep extragalactic fields.

These LRDs are selected as compact JWST/NIRCam F444W sources exhibiting characteristic V-shaped rest-frame continua, typically characterized by red optical slopes and blue ultraviolet slopes (see Method for more details). For a subset of these objects, medium- and high-resolution NIRSpec spectra are available, enabling black hole mass estimates from either broad Hα or Hβ emission lines using standard virial calibrations[46]. To obtain the galaxy sample within the same redshift interval, we draw from the DAWN JWST Archive (DJA) catalogs, which compile robust photometric redshift measurements from multiple public JWST surveys (see Methods for details). The galaxy sample is selected to have well-constrained photometric redshifts and to be matched in depth in NIRCam/F200W to the LRDs in each redshift bin, ensuring a fair comparison between the two populations.

To quantify the large-scale environments of LRDs, we measure the galaxy overdensity within cylindrical volumes centered on each LRD, using a line-of-sight velocity window of $\Delta v = \pm 2500$ km s^{-1}. Due to the limitation of the observing field of view, the maximum projected radii can only reach $\sim 5\ h^{-1}$ cMpc. The overdensity is defined as $\delta = N_{\rm obs}/N_{\rm exp} - 1$, where $N_{\rm obs}$ is the observed number of galaxies and $N_{\rm exp}$ is the expectation from a random distribution within the same volume. The expected counts are estimated using random catalogs that uniformly sample the survey footprints and depths, normalized to the total number of galaxies in each redshift bin. Similarly, we follow the same procedure to calculate the overdensity for the full galaxy sample. We present the overdensity of LRDs and galaxies at $3 < z < 7$ in Figure 1, where the error is estimated from the field-level jackknife method (excluding one field each time). Obviously, the overdensity of LRDs is lower than that of galaxies at $z > 4$ with significance $> 5\sigma$ at all radii and becomes comparable at $3 < z < 4$. This trend extends to the local LRDs at $z \sim 0.1 - 0.2$ identified in a recent study[47] (details in Methods). The ratio of $\delta_{\rm LRD}$ and $\delta_{\rm Galaxy}$ increases rapidly from $z \sim 6.5$ to $z \sim 3.5$, with the significance of the change $> 5\sigma$. This phenomenon demonstrates that LRDs

inhabit under-dense regions at $z > 4$ and subsequently evolve into environments comparable to those of normal galaxies at $3 < z < 4$ and even at $z \sim 0.2$. We note that in a recent study[48], the authors measure the overdensity within a volume of $(15\ h^{-1}\ \mathrm{cMpc})^3$ around five LRD-like sources, together with a larger sample of low-luminosity AGNs at $3.9 < z < 6$. While that work does not explicitly isolate LRDs as a distinct population, it shows that the majority of such sources (four out of five) reside in under-dense regions, as shown in their Table 2 and Figure 2. And their AGN sample has SMBH masses that are, on average, similar to those of our LRDs, with over half residing in under-dense regions.

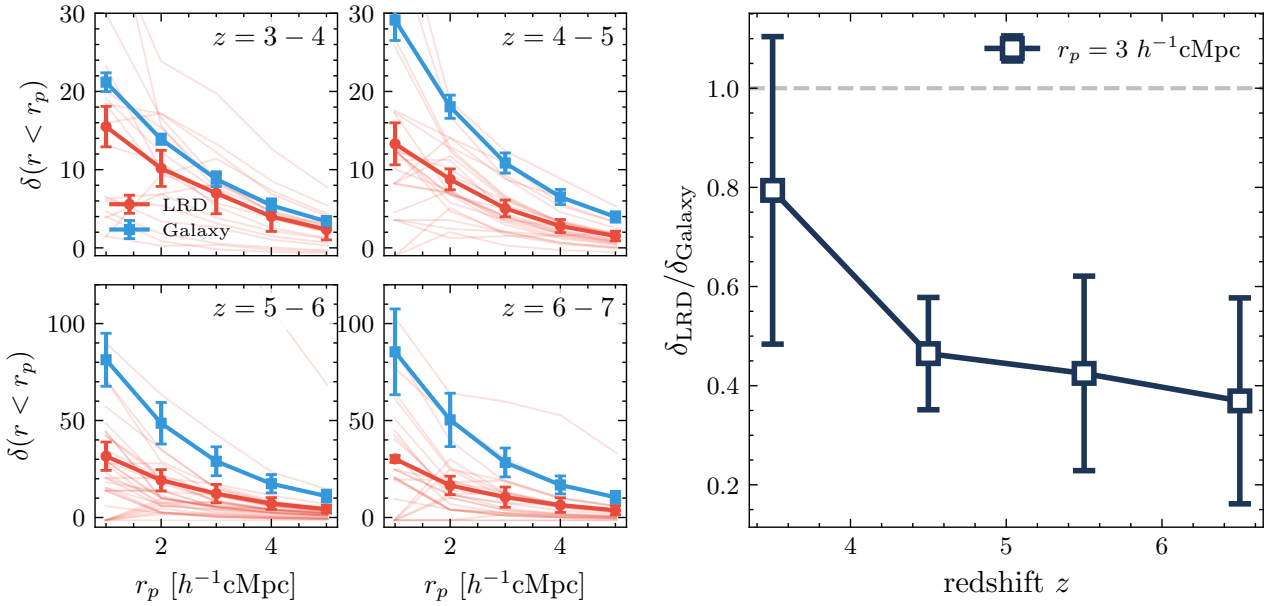

Figure 1. Overdensity of LRDs and galaxies across cosmic time. Left panel: The projected overdensity profiles of LRDs (red) and galaxies (blue) in four redshift bins: $3 < z < 4$, $4 < z < 5$, $5 < z < 6$, and $6 < z < 7$ with 1σ uncertainties derived from the jackknife method, where the overdensity for each LRD is also shown with thin red line. Right panel: The ratio of the overdensity of LRDs to galaxies integrated within $r_p < 3\,h^{-1}$ cMpc as a function of redshift.

The role of dark matter in galaxy formation and evolution is well established, as it not only shapes the large-scale distribution of galaxies but also, through the large-scale environment, plays a key role in the galaxy assembly process[49,50]. Clustering analyses, commonly based on the two-point auto-correlation function[51], have proven to be powerful tools for linking the large-scale properties of galaxies to the small-scale physics, such as their hosting dark matter halos. In this work, we measure the projected cross-correlation function between LRDs and galaxies, as well as the projected autocorrelation function of galaxies in the redshift range of $3 < z < 7$ (see Methods for details). From these measurements, we infer the dark matter halo masses of galaxies and LRDs, as shown in Figure 2. We find that the characteristic dark matter halo mass of LRDs grows rapidly from $\lesssim 10^{10.1}\,M_\odot$ at $z \sim 7.5$ to $\sim 10^{11.3}\,M_\odot$ at $z \sim 3.5$, approaching values of typical massive galaxies or AGNs at the same redshift and thus becoming roughly indistinguishable from them.

The evolution of high-redshift galaxies, AGNs, quasars, and their associated dark matter halos has been extensively explored in recent years with JWST. Clustering analyses reveal that galaxies with $\langle M_{\mathrm{UV}} \rangle \sim -20$, identified as H$\alpha$ or [O III] emitters, reside in dark matter halos of $\sim 10^{11.5}$ M$_\odot$ at $z \sim 4.3$ and $\sim 10^{11.0}$ M$_\odot$ at $z \sim 7.3$[61]. Low-luminosity AGNs at $3.9 < z < 6$ occupy comparable halos as similarly

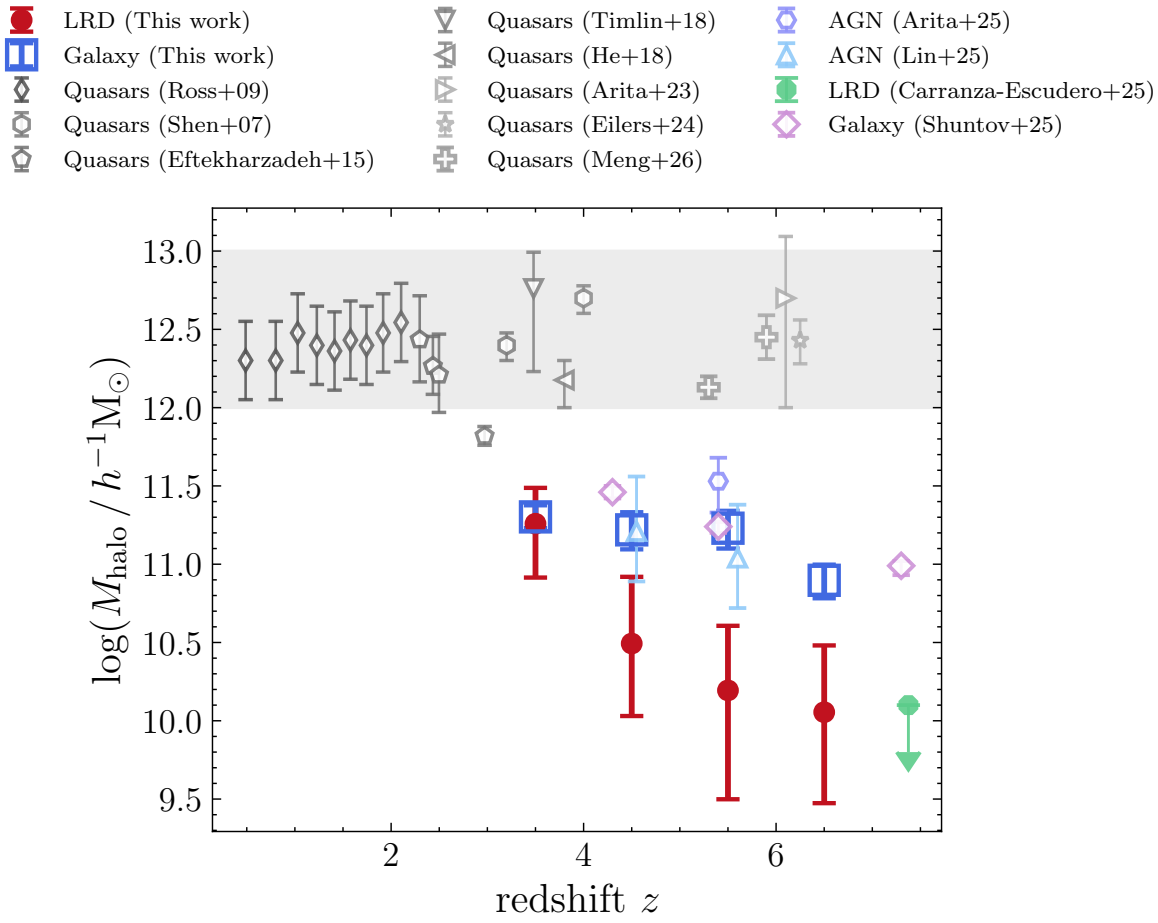

Figure 2. Halo masses of LRDs and comparison samples across cosmic time. The dark matter halo mass ($M_{\rm halo}$) as a function of redshift for various populations. Open blue squares show the galaxies, filled red circles represent LRDs from this work, with downward arrows indicating upper limits. Grey symbols denote quasars from clustering analyses[52–59]. Light blue triangles and violet hexagon show low-luminosity broad-line AGNs from clustering analysis[48,60]. Green symbols represent LRDs from clustering analysis[41]. Purple diamonds indicate spectroscopically confirmed massive galaxies[61]. The grey shaded region marks the typical halo mass range (10^{12}–$10^{13}\,M_\odot$) for typical Type-1 AGN.

luminous galaxies, with $\log_{10}(M_{\rm halo,min}/M_\odot) \simeq 11$–$11.5$[48,60]. In contrast, luminous quasars, whose bolometric luminosities are $\sim 2-3$ orders of magnitude higher than those of such galaxies, low-luminosity AGNs and LRDs, exhibit a minimum host halo mass of $\log_{10}(M_{\rm halo,min}/M_\odot) \simeq 12.4$ at $\langle z\rangle \simeq 6.3$ using five quasar fields[58], and a characteristic mass of $\sim 10^{12.2}\,M_\odot$ at $5.0 < z \leq 5.6$ and $5.6 < z \leq 6.2$ from wide-field quasar auto-correlation measurements[59]. Our inferred halo masses for LRDs are lower than our galaxy sample and the galaxies in the literature[61] at $4 < z < 7$. The halo masses for our general galaxy sample are slightly lower than those reported in the literature[61], as expected given that our galaxies are slightly fainter in general. Furthermore, the derived dark matter halo masses for both galaxies and LRDs are consistent with their measured overdensity, as shown in Figure 1, as expected from clustering theory.

Investigating the correlations among stellar mass, dark matter halo mass, and supermassive black hole mass is crucial for understanding galaxy evolution and the coevolution of SMBHs and their hosts. In this work, we estimate the average stellar masses of LRDs at a given bin of redshift using the $M_* - M_{\rm halo}$

scaling relation derived from UniverseMachine[62]. We present the resulting $M_{\rm halo} - M_{\rm BH}$ and $M_* - M_{\rm BH}$ relation in Figure 3. We find that LRDs at $z > 4$ deviate significantly from the local relation, whereas LRDs at $z \sim 3.5$ lie much closer to the local correlations of both $M_{\rm halo} - M_{\rm BH}$[63–65] and $M_* - M_{\rm BH}$[66], despite still exhibiting clear deviations. This result further supports the conclusion that the SMBH masses of LRDs at $z > 4$ are over-massive compared to local galaxies in the $M_* - M_{\rm BH}$ relation, and that $M_* - M_{\rm BH}$ relation of high-redshift LRDs will evolve to the local relation. Both the $M_{\rm halo} - M_{\rm BH}$ and $M_* - M_{\rm BH}$ relation measured for our LRD sample are well consistent with those in *BRAHMA* cosmological simulation at $5 < z < 8$[67], in which the authors produce mock observations of AGNs and their host galaxies to mimic the observational properties of LRDs. In contrast, the *ASTRID* cosmological simulation does not reproduce the observational $M_* - M_{\rm BH}$ and/or $M_{\rm halo} - M_{\rm BH}$ relation of LRDs over the same redshift range[68]. It should be noted that the adopted empirical $M_* - M_{\rm halo}$ relation from UniverseMachine may not precisely describe LRDs, whose underlying physical nature remains poorly understood. In addition, black hole mass estimates in LRDs are themselves highly uncertain, as the physical origin of the observed broad emission lines remains debated (e.g., virial motion versus electron scattering[29]). If the broad lines are not predominantly virial in origin, the inferred black hole masses could be systematically overestimated by up to ∼1 dex. Even under such a reduction, however, the LRDs at $z > 4$ in our sample would still remain offset above the local $M_{\rm BH}$–$M_{\rm halo}$ scaling relation.

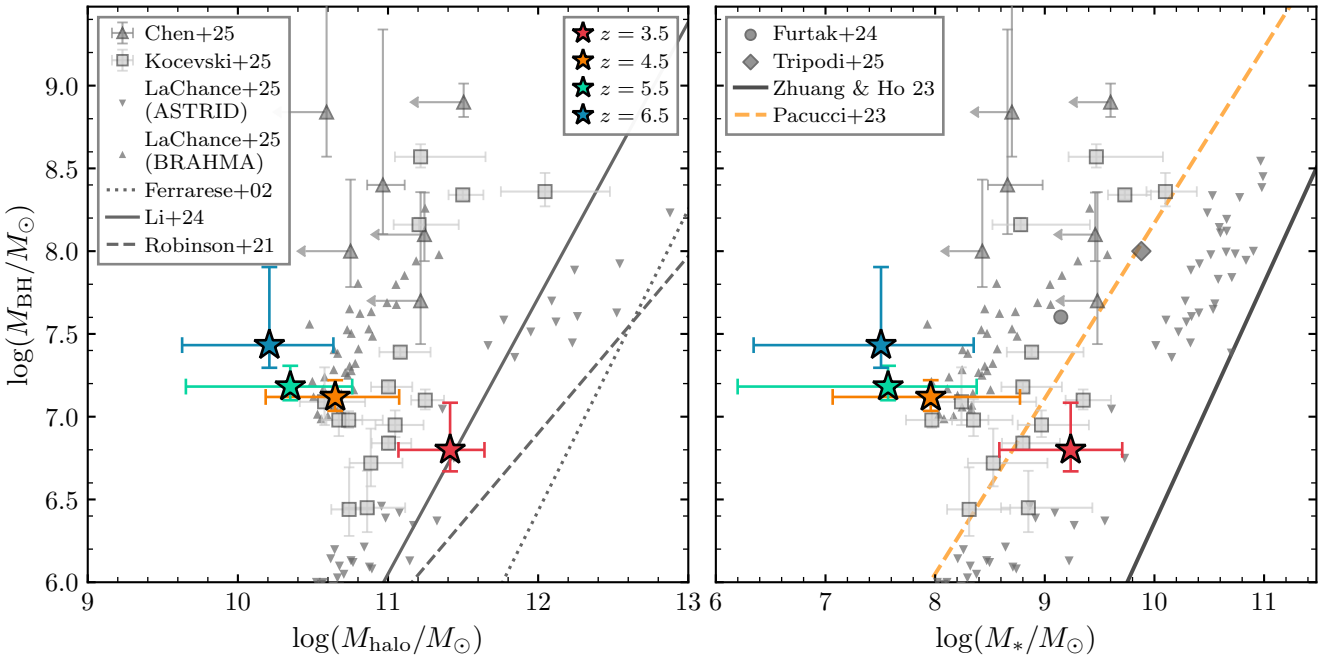

Figure 3. Black hole mass scaling relations for LRDs. Solid stars denote the LRDs in our sample, with different colors indicating different redshift bins. Leftward arrows indicate upper limits on $M_{\rm halo}$ or M_*. Upward triangles show LRDs from Chen et al. (2025)[27], squares represent LRDs from Kocevski et al. (2025)[24], downward triangles and leftward triangles show predictions from the *ASTRID* and *BRAHMA* simulations, respectively[67], and the circle and diamond mark additional LRDs from the Furta et al. (2025)[3] and Tripodi et al. (2025)[25]. In the left panel, the three lines show the local relation[63–65]. In the right panel, the solid black line shows the local relation[66], and the dashed orange line represents the high-z relation[69].

The luminous AGNs or heavy galaxies are typically found in over-dense environments[70], LRDs re-

side preferentially in under-dense regions, where these LRDs are hosted by lower-mass dark matter halos (as shown in Figure 2). This contrast suggests that their formation mechanisms may differ fundamentally from those of typical galaxies and luminous AGNs, as the environment strongly influences galactic merger and accretion histories. We find that the typical halo mass of LRDs increases by more than one order of magnitude from $z \sim 7$ to $z \sim 3$, whereas the average black hole mass shows little evolution over the same redshift interval. By $z \sim 3$, the assembly of dark matter halos and gas reservoirs appears largely complete; at this point, both the halo masses and the $M_{\rm BH} - M_*$ relation become broadly consistent with those of local galaxies, rendering LRDs virtually indistinguishable from the general galaxy population. Moreover, given that virial radius scales with halo mass, galaxies in $\sim 10^{11}\,M_\odot$ halos, whose stellar mass corresponds to $\sim 10^{9.5}\,M_\odot$, would not be as compact as LRDs if they followed normal structural scaling relations[71,72].

The full picture of LRDs' dark matter halo evolution is still ambiguous. Pacucci & Loeb (2025)[69] proposed that low-spin dark matter halos can naturally explain the compactness, abundance, and redshift distribution of LRDs, which is also supported by the possible black hole formation from gravothermal core collapse in self-interacting dark matter halos at high redshift[73]. In this model[69], the effective radius of a galaxy scales as $R_{\rm eff} \propto \lambda\, r_{200}(M_h, z)$, with λ denoting the halo spin parameter. Consequently, the extreme compactness of LRDs arises naturally from their unusually low halo spins ($\lambda \sim 0.01$), corresponding to approximately the lowest $\sim 1\%$ of the spin distribution. As LRD host halos grow from $\sim 10^{10.0}\,M_\odot$ to $\sim 10^{11.5}\,M_\odot$, newly accreted material from the cosmic web carries angular momentum and λ increases. With an increase of λ to several percent(e.g., $\lambda \gtrsim 0.03$), $R_{\rm eff}$ grows up to $\sim 1\,$kpc, aligning with the typical sizes of normal galaxies at $3 < z < 4$[71,72] and thereby eliminating the structural compactness that defines LRDs. Furthermore, the baryons will easily concentrate into an extremely dense core in low-spin halos, which will lead to compact stellar distribution and high gas density as constrained from the possible Balmer features as found in many LRDs[9]. The compact dense gas core may be the physical reason for the V-shaped SEDs in LRDs[14], where the V-shaped SED will disappear if the gas distribution is not compact. Moreover, the starlight from the elevated star formation of the galaxies would significantly disturb the V-shaped SEDs in LRDs.

Methods

Data Sample

We construct the LRD sample by combining three recent spectroscopically confirmed JWST LRD catalogs spanning $z \sim 2$–9. One sample is drawn from Zhang et al. (2026)[44], which identified 98 LRDs from JWST/NIRCam and NIRSpec observations across six deep fields: A2744, CEERS, GOODS-S, GOODS-N, COSMOS, and UDS[74–77]. These sources were selected as compact NIRCAM/F444W objects exhibiting characteristic V-shaped rest-frame continua, defined primarily by $\beta_{\rm opt} > 0$ and $\beta_{\rm UV} < -0.37$, with continuum slopes corrected for emission-line contamination using NIRSpec/PRISM spectroscopy. The other sample of de Graaff et al. (2025)[45], identified 116 high-purity LRDs from $\sim$ 17,000 high-quality NIRSpec/PRISM spectra using statistically robust V-shaped continuum criteria ($\beta_{\rm opt} > 0$, $\beta_{\rm UV} < -0.2$, and $\beta_{\rm UV} - \beta_{\rm opt} > 0.5$ at $> 95\%$ confidence) together with compact F444W morphologies. Also, we include the RUBIES spectroscopic sample of Hviding et al. (2025)[7], consisting of 36 LRDs identified through joint PRISM+G395M fitting and broad Balmer-line detections, all of which also exhibit compact morphologies and V-shaped continua. The final merged sample consists of 170 unique LRDs at $2 < z < 9$ after removing duplicate sources across the three catalogs. Restricting the sample to the six deep fields described above, in which the clustering analyses could be conducted, and the redshift range $3 < z < 7$ yields 98 LRDs used in our analysis.

The LRDs' absolute magnitude at 1450 Å, M_{1450}, is derived from the mean spectral flux density measured over $1425-1475$ Å using the DAWN JWST Archive (DJA) public NIRSpec/PRISM dataset (v4)[78], as shown in Figure 4. Only sources with reliable spectroscopic coverage of the rest-frame UV continuum are included in this measurement. The majority of the LRD sample is quite faint, and the distribution of M_{1450} v.s. z for our LRDs are consistent with the literature distribution[24]. The number of LRDs at $z < 3$ and the number of galaxies at $z > 7$ are both very limited. Therefore, we only focus on LRDs in the redshift intervals $z = 3-4$, $4-5$, $5-6$, and $6-7$, which contain 16, 24, 33, and 25 sources, respectively. All LRDs used in the final analysis have spectroscopic redshifts For a subset of these sources, NIRSpec medium- and high-resolution grating spectra are available in the DJA Public NIRSpec datasets (v4)[78], which are used to estimate the black hole masses by fitting the broad Hα or Hβ emission lines and applying the virial mass calibration according to the well-established scaling relation[46]. We caution that these estimates may be subject to systematic uncertainties associated with the physical origin of the line broadening[29], which could affect the absolute normalization of $M_{\rm BH}$ by $\sim$1 dex.

Similar to a recent study[60], we construct our galaxy sample at the same redshift range from the DJA catalogs. The DJA catalogs are built from publicly available JWST survey data processed by the Cosmic Dawn Center using the `grizli`[79] and `msaexp`[80] pipelines. Photometric redshifts are estimated with `EAZY`[81] based on combined JWST and HST photometry. We utilize the DJA v7 catalogs from four survey fields: the Cosmic Evolution Early Release Science Survey (CEERS)[75], the JWST Advanced Deep Extragalactic Survey (JADES)[76], the Public Release Imaging for Extragalactic Research (PRIMER) survey[77], and the Ultradeep NIRSpec and NIRCam Observations Before the Epoch of Reionization (UNCOVER) survey[74]. All UNCOVER galaxies are corrected for gravitational lensing magnification using the v2.0 lensing models[82,83]

The selection of the galaxy sample is based on two criteria: the uncertainty of photometric redshift estimated using `EAZY` for each source is less than 0.5, $\delta z_{\rm phot} < 0.5$, and redshift estimates must be based on at least 12 photometric filters ($n_{\rm filter} \geq 12$), to ensure robust redshift estimation. As demonstrated in the literature[84], the photometric redshift estimation is quite reliable and robust. Of the 17636 galaxy samples, 727 have spectroscopic redshifts. We use spectroscopic redshifts wherever they are available for the galaxy sample. Only when spectroscopic redshifts are unavailable do we rely on photometric

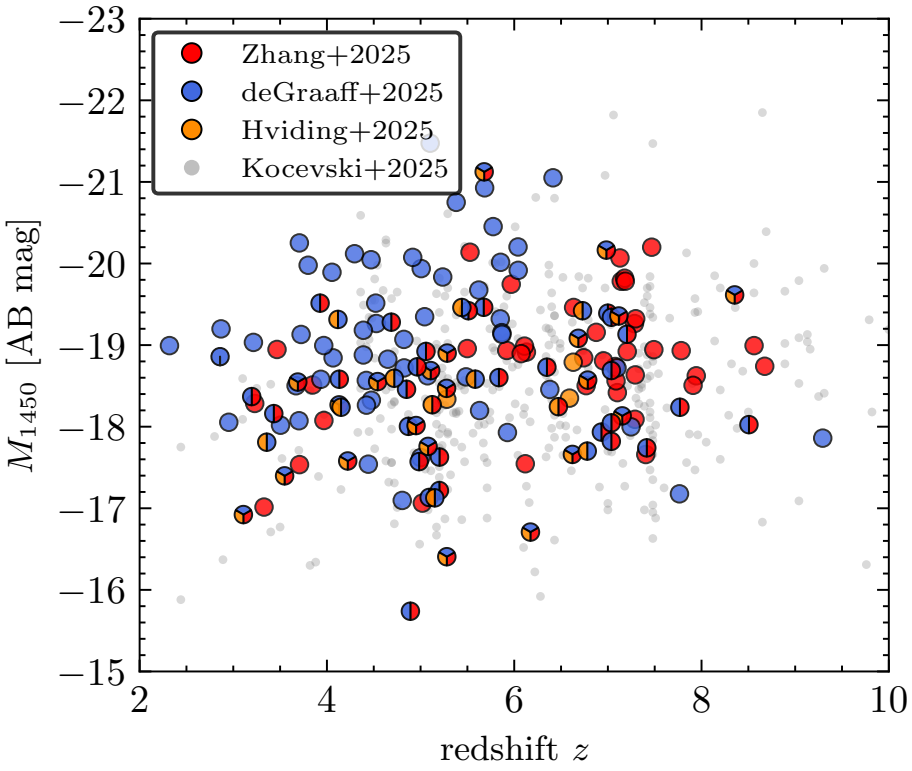

Figure 4. Redshift and absolute magnitude distributions of LRDs. The distributions of redshift and absolute magnitude at 1450 Å (M_{1450}) for LRDs in the redshift range of $2.0 < z < 10$ are shown. Red circles indicate the LRDs in our sample, while small grey dots represent LRDs compiled from the literature[24]

redshifts. The comparison between photometric and spectroscopic redshifts is shown in Figure 5. Here we adopt a stricter criterion ($|\Delta z|/(1+z) > 0.1$) for outliers, which account for only 6.60% of the entire spectroscopic sample, demonstrating the reliability and robustness of photometric redshift estimation.

Photometry of all sources is measured within a circular aperture with a diameter of 0.5″. In each redshift bin, we further restrict the NIRCam/F200W magnitudes of the galaxy sample to be within ±1 mag of the median F200W magnitude of the LRD sample. This cut is applied to ensure that the effective detection depths of the two populations are comparable, thereby enabling a fair comparison between them. Our galaxy sample lies well within the high-completeness regime of the JWST surveys. As shown in Figure 4 of Marlin Merlin et al. (2024)[85], the majority of the fields achieve $> 90\%$ completeness at ~ 29 mag, significantly fainter than the magnitude range considered in our analysis, indicating that incompleteness effects should be minimal for both samples. We additionally confirmed that our main results remain unchanged after excluding the relatively shallow UDS field from the analysis.

A random sample is essential for large-scale clustering analysis. We build the random catalogs following Arita et al. (2025)[60], with a surface number density of 100 arcmin^{-2} uniformly distributed over the survey regions. To accurately trace the survey geometry and depth variations, we retain only random points within the footprint that have $n_{\rm filter} \geq 12$ and NIRCan/F444W observations available. The redshifts of the random points are assigned to match the redshift distribution of the galaxy sample. The constructed random catalog properly inherits the above properties of the galaxy catalog. This random catalog is then used in the estimation of both the overdensity and the two-point correlation function.

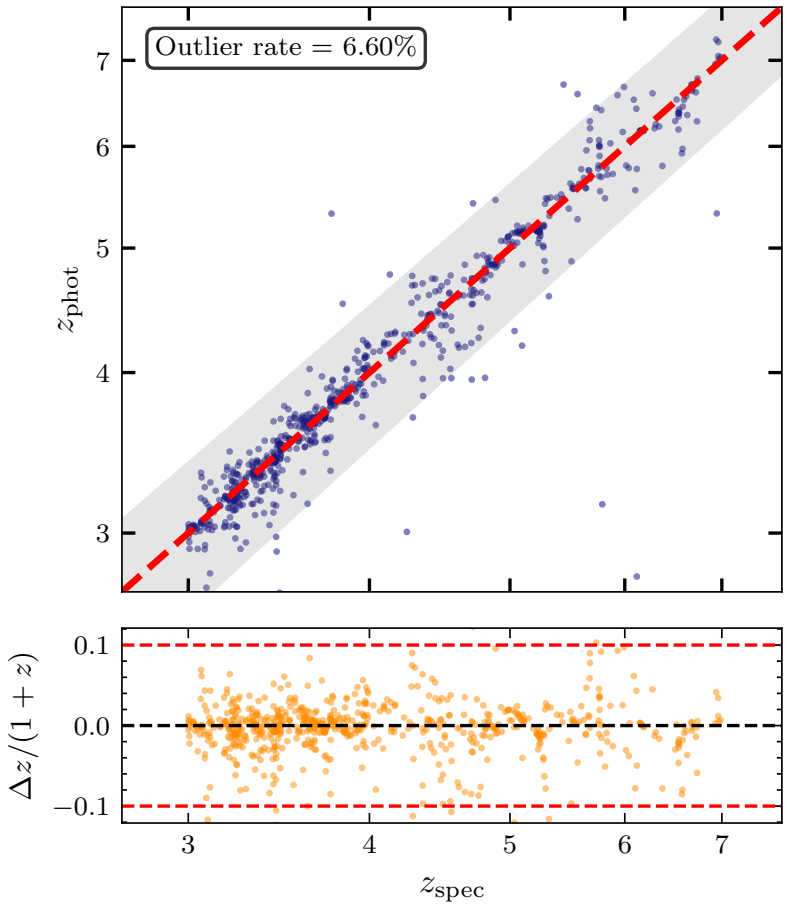

Figure 5. Photometric versus spectroscopic redshift for galaxies. Top panel: Comparison between photometric redshift ($z_{\rm phot}$) and spectroscopic redshift ($z_{\rm spec}$) for the galaxy sample across redshift range of $z = 3-7$. The dashed red line displays the 1:1 relation, and the grey shaded region denotes $|\Delta z|/(1+z) < 0.1$. Bottom panel: Normalized redshift residuals $\Delta z/(1+z) = (z_{\rm phot} - z_{\rm spec})/(1+z_{\rm spec})$ as a function of spectroscopic redshift. Horizontal dashed lines mark $\Delta z/(1+z) = 0$ (black) and ± 0.1 (red). The outliers are defined as sources with $|\Delta z|/(1+z) > 0.1$.

We note that there are three local analogs at $z \approx 0.1-0.2$ identified in a recent study[47]. These objects are identified through template matching to the high-redshift LRD spectra, combined with compact morphology and spectroscopic properties. To explore the large-scale environments of those three local LRDs, we collect the galaxy sample and the random sample from the large-scale structure (LSS) clustering catalogs, which are constructed from Dark Energy Spectroscopic Instrument (DESI)[86,87] Data Release 1 (DR1)[88]. The LSS galaxy samples mainly include the Bright Galaxy Sample (BGS) optimized for low-redshift studies[89,90]. These catalogs include the observed galaxy positions together with the associated random catalogs, as well as redshifts and survey completeness weights, enabling three-dimensional clustering and environment measurements[89]. We also incorporate the Sloan Digital Sky Survey (SDSS) Data Release 12 (DR12) BOSS LOWZ large-scale structure catalog, which consists of luminous red galaxies at $z \lesssim 0.4$ and the corresponding random catalog.

Considering that both DESI DR1 and SDSS DR12 around those three local LRDs have low survey coverage, we further supplement the spectroscopic data with the DESI Imaging Legacy Surveys (LS) Data Release 10 (DR10) photometric redshift (photo-z) sweeps catalogs, which provide homogeneous

photometric redshift estimates for galaxies over the DESI Imaging Legacy Surveys footprint[91,92]. To ensure consistency with the official LS DR10 photo-z catalog, we apply the recommended selection criteria for the i-band extended photo-z sample. Objects are required to have at least one exposure in each of the g, r, i, and z bands ($N_{\mathrm{OBS_{G,R,I,Z}}} \geq 1$), and only sources with z-band magnitude brighter than 21 are considered reliable. Additionally, we require a photo-z uncertainty of $\sigma_z < 0.02$ to ensure high-quality redshift estimates. For star-galaxy separation, we exclude point sources (TYPE = 'PSF') and apply an optical-WISE color cut ($r - W1 > 0.5$) to preferentially select galaxies, following Zhou et al. (2021)[93]. To ensure a consistent comparison, we apply the apparent g-band magnitude cut, $20.0 < g < 21.5$, to both the spectroscopic and photometric samples, to match the apparent magnitudes of the three LRDs. Also, for the LS DR10 photo-z sweeps catalog, we force the redshift distribution of the random catalog to be matched to that of the real galaxies.

ENVIRONMENTS

To quantify the large-scale environments of our JWST LRD sample, we calculate the galaxy overdensity, δ, within cylindrical volumes centered on each LRD. Specifically, we count galaxies within projected radii of $r_p = 1$, 2, 3, 4, and 5 h^{-1} cMpc and within a line-of-sight velocity range of $\Delta v = \pm 2500$ km s^{-1}. We have verified that varying the velocity window almost does no affect the results. The overdensity is defined as $\delta(r_p) = \frac{N_{\mathrm{obs}}(r_p)}{N_{\mathrm{exp}}(r_p)} - 1$, where $N_{\mathrm{obs}}(r_p)$ is the number of galaxies within the given cylindrical volume, and $N_{\mathrm{exp}}(r_p)$ is the expected number of galaxies for the random distribution within the same volume. To calculate N_{exp}, we count the number of random points within the same cylindrical volume and scale it by the normalization factor $N_{\mathrm{total\ galaxy}}/N_{\mathrm{total\ random}}$. We follow the same procedure to compute the overdensity distribution of the full galaxy sample in the same redshift range.

To estimate the uncertainty in the overdensity parameter δ, we employ a jackknife resampling technique. We recompute the mean overdensity $\langle\delta\rangle$ by sequentially excluding one JWST field at a time, yielding N jackknife realizations, where N is the number of fields. The jackknife variance is then computed as

$$\sigma^2 = \frac{N-1}{N} \sum_{i=1}^{N} \left(\langle\delta\rangle_i - \langle\delta\rangle\right)^2, \tag{1}$$

where $\langle\delta\rangle_i$ is the measurement excluding the i-th field. We report the square root of this variance as the uncertainty.

To investigate the environments of the three local LRDs, whose SMBH masses are all around $10^{6.5}$ $M_\odot$, we apply the method described above to the DESI and SDSS large-scale structure catalogs. Given the limited spectroscopic sky coverage in their vicinity, we measure their overdensity within a volume of ($30\,h^{-1}$ Mpc^3) to mitigate this constraint, as shown in Figure 6. We further complement the spectroscopic data with the LS DR10 photo-z data due to the low sky coverage around these three local LRDs. For comparison, the galaxy samples shown in Figure 6 are constructed by randomly selecting 500 galaxies from the DESI DR1 footprint for spectroscopic analysis and an additional 500 galaxies from the LS DR10 catalog for photometric redshift analysis. Given the uniform coverage of these surveys and the random selection of galaxy control samples, the overdensity measurements for these control galaxies are not significantly affected by survey incompleteness or edge effects. The resulting large-scale environments of these three local LRDs are comparable to those of typical galaxies within the measurement uncertainties.

Clustering Analysis

We evaluate the projected cross-correlation function between the LRDs and the galaxies of our sample, $\omega_{\mathrm{p,CCF}}(r_{\mathrm{p}})$, and the projected autocorrelation function of the galaxies, $\omega_{\mathrm{p,ACF}}(r_{\mathrm{p}})$. The projected

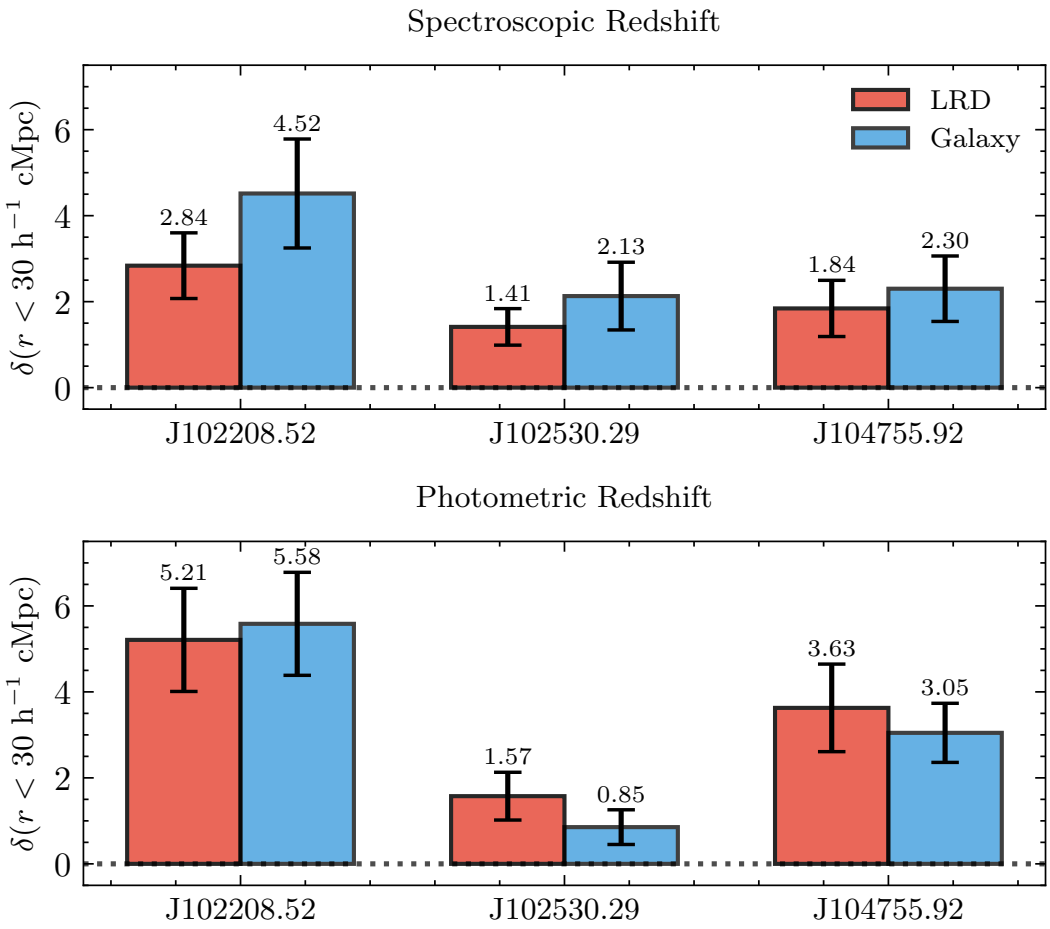

Figure 6. Overdensity of the three local LRDs and galaxies within a volume of (30 h^{-1} cMpc)^3. Top panel: overdensity measurements within a volume of (30 h^{-1} cMpc)^3 around the three local LRDs (red bars) and the galaxy sample (blue bars), using spectroscopic data from the combined SDSS and DESI surveys. Bottom panel: overdensity measurements using the photometric redshift catalog. Error bars represent 1σ uncertainties derived from jackknife resampling for LRDs and galaxies, and the numbers are the values of the overdensity measurements.

correlation functions are obtained by integrating the three-dimensional correlation functions, $\xi_{\mathrm{CCF}}(r_\mathrm{p},\pi)$ and $\xi_{\mathrm{ACF}}(r_\mathrm{p},\pi)$, where r_p and π represent the transverse and line-of-sight separations, respectively.

There are various estimators to determine the projected correlation function, and we adopt the Landy & Szalay estimator[94], defined as follows:

$$\omega_{\mathrm{p,CCF/ACF}}(r_\mathrm{p}) = \int_{-\pi_{\mathrm{cut}}}^{\pi_{\mathrm{cut}}} \xi_{\mathrm{CCF/ACF}}(r_\mathrm{p},\pi)\, d\pi, \tag{2}$$

where π_{cut} is the maximum line-of-sight separation, fixed to 100 h^{-1}Mpc. The estimators for the cross- and auto-correlation functions are given by

$$\xi_{\mathrm{CCF}}(r_\mathrm{p},\pi) = \frac{D_\mathrm{L}D_\mathrm{G} - D_\mathrm{L}R_\mathrm{G} - D_\mathrm{G}R_\mathrm{L} + R_\mathrm{L}R_\mathrm{G}}{R_\mathrm{L}R_\mathrm{G}}, \tag{3}$$

$$\xi_{\mathrm{ACF}}(r_\mathrm{p},\pi) = \frac{D_\mathrm{G}D_\mathrm{G} - 2D_\mathrm{G}R_\mathrm{G} + R_\mathrm{G}R_\mathrm{G}}{R_\mathrm{G}R_\mathrm{G}}. \tag{4}$$

Here D and R denote the data and random catalogs, respectively, and the subscripts indicate the corresponding samples. The random catalogs are described above. All pair counts are normalized by the total number of possible pairs in each sample. The uncertainties of the projected correlation function are estimated using a leave-one-out jackknife resampling method. Specifically, for the sample of LRDs, we recompute each time, excluding one LRD from the sample, and derive the uncertainties from the variance among these jackknife realizations.

The projected correlation function is derived from the integration of the real-space correlation function $\xi(r)$[95] as follows:

$$\omega_{\rm p}(r_{\rm p}) = 2\int_{r_{\rm p}}^{\infty} \frac{r\,\xi(r)}{\sqrt{r^2 - r_{\rm p}^2}}\,dr. \tag{5}$$

Assuming a power-law function for the real-space correlation function, $\xi(r) = (r/r_0)^{-\gamma}$, the projected correlation function can be written as

$$\omega_{\rm p}(r_{\rm p})\,r_{\rm p} = {\rm B}\left(\frac{\gamma-1}{2}, \frac{1}{2}\right)\left(\frac{r_{\rm p}}{r_0}\right)^{-\gamma}, \tag{6}$$

where B denotes the beta function.

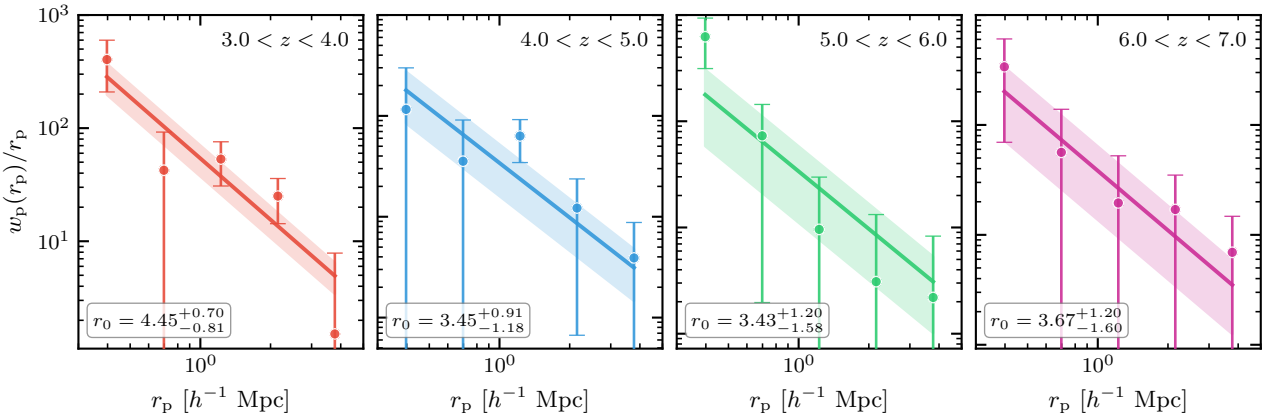

Figure 7. Projected cross-correlation functions between LRDs and galaxies. The projected cross-correlation function $\omega_{\rm p}(r_{\rm p})$ as a function of projected separation $r_{\rm p}$ for four redshift bins: $3.0 < z < 4.0$ (left), $4.0 < z < 5.0$ (second from left), $5.0 < z < 6.0$ (second from right), and $6.0 < z < 7.0$ (right). Colored circles with error bars represent the measured projected cross-correlation function between LRDs and surrounding galaxies. 1σ error is obtained from a jackknife method. Solid lines show the best-fit power-law models with $\gamma = 1.8$, and shaded regions indicate the 1σ uncertainty in the correlation length r_0. The best-fit correlation lengths are displayed in each panel.

Figure 7 shows the projected cross-correlation function between galaxies and LRDs, and Figure 8 displays the projected autocorrelation of galaxies for the different redshift intervals. The solid lines indicate the best-fit power-law models with $\gamma = 1.8$ fixed, and the shaded regions indicate the 1σ uncertainty obtained from the Markov Chain Monte Carlo (MCMC) method.

Halo mass of galaxies and LRDs

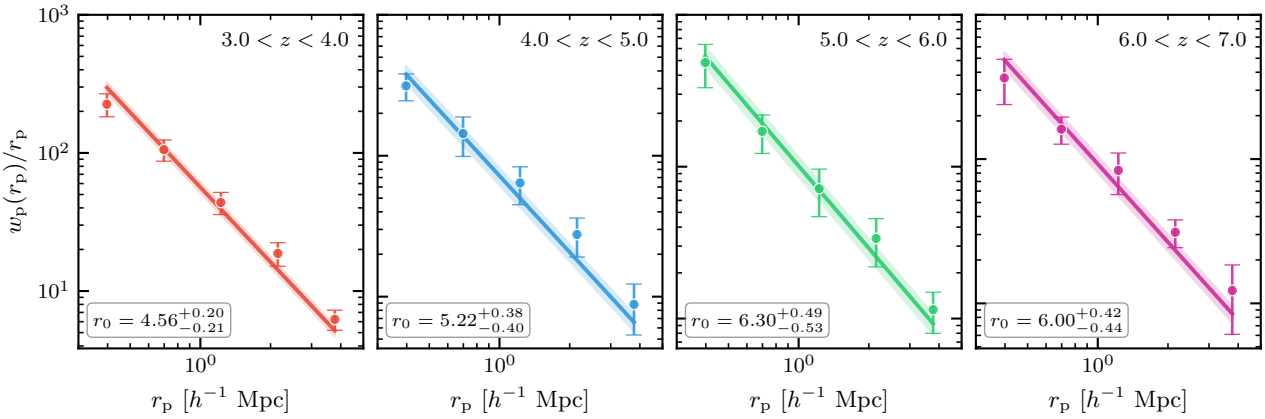

Figure 8. Projected auto-correlation function of galaxies. Same as the figure 7, but for the projected auto-correlation function $\omega_p(r_p)$ of the galaxy.

We estimate the typical dark matter halo (DMH) masses of the LRDs from the clustering measurements obtained above. The large-scale linear bias parameter quantifies how strongly objects cluster relative to the underlying dark matter distribution. We define the bias at a reference scale of $r_{\rm ref} = 8\,h^{-1}$ Mpc as

$$b = \sqrt{\frac{\xi_{\rm obs}(r_{\rm ref}, z)}{\xi_{\rm DM}(r_{\rm ref}, z)}}, \tag{7}$$

where $\xi_{\rm obs}(r, z)$ is the observed correlation function and $\xi_{\rm DM}(r, z)$ is the dark matter correlation function at redshift z.

As discussed above, we have adopted the power-law function for the observed correlation function. The dark matter correlation function $\xi_{\rm DM}(r, z)$ is computed using the `halomod` package[96,97]. We adopt the well-established halo bias model[98], a linear matter power spectrum generated with `CAMB` package[99], and the well-known linear growth model[100]. Following the standard relation between auto- and cross-correlation functions[101], and assuming power-law forms for all correlation functions, we could obtain the linear bias for LRDs:

$$\xi_{\rm LRD,LRD}(r) = \frac{\xi^2_{\rm LRD,gal}(r)}{\xi_{\rm gal,gal}(r)}, \tag{8}$$

where $\xi_{\rm LRD,gal}(r)$ is the LRD-galaxy cross-correlation function and $\xi_{\rm gal,gal}(r)$ is the galaxy autocorrelation function, from which we could derive the effective correlation length $r_{0,\rm LRD}$ and the bias parameter $b_{\rm LRD}$ for LRDs. The halo mass corresponding to a given bias parameter is obtained by inverting the halo bias − halo mass relation. We use the `colossus` implementation of the well-developed halo bias model[98] with a halo mass definition of $M_{\rm 200m}$. The clustering results are presented in Table 1.

The M_* of LRDs

To infer the stellar masses corresponding to our halo mass measurements, we adopt the redshift-dependent stellar-to-halo mass relation (SMHM) from UniverseMachine[62,102]. This formalism parametrizes the median stellar mass as a function of halo mass and redshift via the following equation:

$$\log M_*(M_{\rm h}, z) = \log(\varepsilon M_1) + f\left(\log \frac{M_{\rm h}}{M_1}\right) - f(0), \tag{9}$$

Table 1. Best-fit parameters. Best-fit correlation lengths, galaxy bias factors, and inferred dark matter halo masses measured from galaxy auto-correlation functions (ACF) and LRD–galaxy cross-correlation functions (CCF) in different redshift bins. $N_{\rm LRD}$ and $N_{\rm galaxy}$ denote the number of LRDs and photometric galaxies used in each bin.

Redshifts	$N_{\rm LRD}$	$N_{\rm galaxy}$	$r_{0,\rm CCF}$ (h^{-1} Mpc)	$r_{0,\rm ACF}$ (h^{-1} Mpc)	$b_{\rm galaxy}$	$b_{\rm LRD}$	$\log(M_{\rm halo,galaxy})$ ($h^{-1}\mathrm{M}_\odot$)	$\log(M_{\rm halo,LRD})$ ($h^{-1}\mathrm{M}_\odot$)
$3-4$	16	6431	$4.45^{+0.70}_{-0.81}$	$4.56^{+0.20}_{-0.21}$	$3.01^{+0.13}_{-0.12}$	$2.94^{+0.40}_{-0.47}$	$11.30^{+0.07}_{-0.07}$	$11.26^{+0.23}_{-0.34}$
$4-5$	24	5408	$3.45^{+0.91}_{-1.18}$	$5.22^{+0.38}_{-0.40}$	$4.17^{+0.28}_{-0.28}$	$2.85^{+0.83}_{-0.64}$	$11.22^{+0.11}_{-0.12}$	$10.49^{+0.43}_{-0.46}$
$5-6$	33	2550	$3.43^{+1.29}_{-1.58}$	$6.30^{+0.49}_{-0.53}$	$5.84^{+0.41}_{-0.44}$	$3.35^{+1.10}_{-1.23}$	$11.23^{+0.11}_{-0.13}$	$10.19^{+0.41}_{-0.70}$
$6-7$	25	1293	$3.67^{+1.20}_{-1.60}$	$6.00^{+0.42}_{-0.44}$	$6.41^{+0.39}_{-0.41}$	$4.11^{+1.26}_{-1.33}$	$10.90^{+0.10}_{-0.11}$	$10.05^{+0.43}_{-0.58}$

where the function $f(x)$ is defined as:

$$f(x) = -\log\left(10^{\alpha x}+1\right) + \delta\frac{\left(\log\left(1+e^{x}\right)\right)^{\gamma}}{1+e^{-x}}, \quad x = \log\frac{M_{\rm h}}{M_1}, \tag{10}$$

with α controlling the low-mass slope ($M_* \propto M_{\rm h}^{\alpha}$ at low halo masses), and δ and γ jointly regulating the curvature and amplitude at the high-mass end. These shape parameters (α, δ, γ), along with the characteristic halo mass M_1 and normalization ε, evolve with redshift as given by Equations (3)–(5) in the paper[102] and M_1 and ε represent the characteristic halo mass and normalization, respectively.

We note that although UniverseMachine was calibrated using pre-JWST observations, the SMHM relation remains robust across the mass range we explored. Recent JWST studies[103,104] suggest a higher SMHM ratio at $z \gtrsim 4$ at the high-mass end, implying enhanced star-formation efficiency in the early Universe. However, for the halo mass range relevant to our sample ($M_{\rm halo} < 10^{11.5}\,M_\odot$ for $z < 5$, and $M_{\rm halo} \lesssim 10^{11.0}\,M_\odot$ for $z > 5$), the difference remains modest, with stellar masses differing by only $0.1-0.2$ dex even at $z \sim 7$.

Acknowlegements

CZ, HZ, and QW acknowledge the financial support from the National Science Foundation of China grant (No. 12303007, 12533005, 12233007) and the China Manned Space Program (CMS-CSST-2025-A06, CMS-CSST-2025-A07). We acknowledge Linhua Jiang and Zijian Zhang for providing the LRD sample.

Author Contributions

HZ designed the project. CZ led the data analysis and HZ provided the guidance. CZ, HZ, and QW led the manuscript writing. QW and HZ led the interpretation of the results. All authors (CZ, HZ, QW, LH, JW) contribute to the discussion and manuscript revision.

Data Availability

The reduced JWST data underlying this study are publicly available through the DAWN JWST Archive (DJA; https://dawn-cph.github.io/dja/). All raw JWST imaging and spectroscopic data used in this work are publicly available from the Mikulski Archive for Space Telescopes (MAST) under their respective survey program IDs. Specifically, the JWST data were obtained from the following public programs and survey fields: the JWST Advanced Deep Extragalactic Survey (JADES; Program IDs 1181 and 1210), The Public Release Imaging for Extragalactic Research survey (PRIMER; Program

ID 4233), The Cosmic Evolution Early Release Science Survey (CEERS; Directors Discretionary Early Release Science Program ID ERS-1345), and the Ultradeep NIRSpec and NIRCam Observations Before the Epoch of Reionization survey (UNCOVER; Program ID GO-2561). The DESI DR1 LSS catalogs and Imaging Legacy Survey Data Release 10 catalogs are publicly available at https://data.desi.lbl.gov. The SDSS DR12 data products are publicly available at https://data.sdss.org/sas/dr12/boss/lss/.

Code Availability

All software packages used in this analysis are publicly available. Specifically, `halomod`[96,97], `CAMB`[99], and `colossus`[98] can be obtained from their respective public repositories.

Competing interests

The authors declare no competing interests.

Correspondence

Correspondence and requests for materials should be addressed to huanian@hust.edu.cn and qwwu@hust.edu.cn.

References

1. Labbé, I. et al. A population of red candidate massive galaxies 600 Myr after the Big Bang. Nature **616**, 266–269, DOI: 10.1038/s41586-023-05786-2 (2023). 2207.12446.

2. Harikane, Y. et al. A JWST/NIRSpec First Census of Broad-line AGNs at z = 4-7: Detection of 10 Faint AGNs with M $_{BH}$ 10^6-10^8 M $_\odot$ and Their Host Galaxy Properties. Astrophys. J. **959**, 39, DOI: 10.3847/1538-4357/ad029e (2023). 2303.11946.

3. Furtak, L. J. et al. A high black-hole-to-host mass ratio in a lensed AGN in the early Universe. Nature **628**, 57–61, DOI: 10.1038/s41586-024-07184-8 (2024). 2308.05735.

4. Greene, J. E. et al. UNCOVER Spectroscopy Confirms the Surprising Ubiquity of Active Galactic Nuclei in Red Sources at z > 5. Astrophys. J. **964**, 39, DOI: 10.3847/1538-4357/ad1e5f (2024). 2309.05714.

5. Matthee, J. et al. Little Red Dots: An Abundant Population of Faint Active Galactic Nuclei at z $\sim$ 5 Revealed by the EIGER and FRESCO JWST Surveys. Astrophys. J. **963**, 129, DOI: 10.3847/1538-4357/ad2345 (2024). 2306.05448.

6. Kokorev, V. et al. A Census of Photometrically Selected Little Red Dots at 4 < z < 9 in JWST Blank Fields. Astrophys. J. **968**, 38, DOI: 10.3847/1538-4357/ad4265 (2024). 2401.09981.

7. Hviding, R. E. et al. RUBIES: A spectroscopic census of little red dots: All point sources with v-shaped continua have broad lines. Astron. Astrophys. **702**, A57, DOI: 10.1051/0004-6361/202555816 (2025). 2506.05459.

8. Setton, D. J. et al. Little Red Dots at an Inflection Point: Ubiquitous V-shaped Turnover Consistently Occurs at the Balmer Limit. Astrophys. J. **995**, 118, DOI: 10.3847/1538-4357/ae1500 (2025). 2411.03424.

9. Wang, B. et al. RUBIES: Evolved Stellar Populations with Extended Formation Histories at z $\sim$ 7–8 in Candidate Massive Galaxies Identified with JWST/NIRSpec. Astrophys. J. Lett. **969**, L13, DOI: 10.3847/2041-8213/ad55f7 (2024). 2405.01473.

10. D'Eugenio, F. et al. BlackTHUNDER strikes twice: rest-frame Balmer-line absorption and high Eddington accretion rate in a Little Red Dot at $z = 7.04$. arXiv e-prints arXiv:2503.11752, DOI: 10.48550/arXiv.2503.11752 (2025). 2503.11752.

11. Ananna, T. T., Bogdán, Á., Kovács, O. E., Natarajan, P. & Hickox, R. C. X-Ray View of Little Red Dots: Do They Host Supermassive Black Holes? Astrophys. J. Lett. **969**, L18, DOI: 10.3847/2041-8213/ad5669 (2024). 2404.19010.

12. Yue, M. et al. Stacking X-Ray Observations of "Little Red Dots": Implications for Their Active Galactic Nucleus Properties. Astrophys. J. Lett. **974**, L26, DOI: 10.3847/2041-8213/ad7eba (2024). 2404.13290.

13. Inayoshi, K. & Maiolino, R. Extremely Dense Gas around Little Red Dots and High-redshift Active Galactic Nuclei: A Nonstellar Origin of the Balmer Break and Absorption Features. Astrophys. J. Lett. **980**, L27, DOI: 10.3847/2041-8213/adaebd (2025). 2409.07805.

14. Inayoshi, K. & Ho, L. C. A Critical Evaluation of the Physical Nature of the Little Red Dots. arXiv e-prints arXiv:2512.03130, DOI: 10.48550/arXiv.2512.03130 (2025). 2512.03130.

15. Ji, X. et al. BlackTHUNDER A non-stellar Balmer break in a black hole-dominated little red dot at z = 7.04. Mon. Not. R. Astron. Soc. **544**, 3900–3935, DOI: 10.1093/mnras/staf1867 (2025). 2501.13082.

16. Chen, K., Li, Z., Inayoshi, K. & Ho, L. C. Dust Budget Crisis in Little Red Dots. Astrophys. J. Lett. **994**, L42, DOI: 10.3847/2041-8213/ae1955 (2025). 2505.22600.

17. Delvecchio, I. et al. Active galactic nuclei-heated dust revealed in "little red dots". Astron. Astrophys. **704**, A313, DOI: 10.1051/0004-6361/202557164 (2025). 2509.07100.

18. Li, Z., Inayoshi, K., Chen, K., Ichikawa, K. & Ho, L. C. Little Red Dots: Rapidly Growing Black Holes Reddened by Extended Dusty Flows. Astrophys. J. **980**, 36, DOI: 10.3847/1538-4357/ada5fb (2025). 2407.10760.

19. Xiao, M. et al. No [C II] or dust detection in two Little Red Dots at z_{spec}> 7. Astron. Astrophys. **700**, A231, DOI: 10.1051/0004-6361/202554361 (2025). 2503.01945.

20. Setton, D. J. et al. A Confirmed Deficit of Hot and Cold Dust Emission in the Most Luminous Little Red Dots. Astrophys. J. Lett. **991**, L10, DOI: 10.3847/2041-8213/ade78b (2025). 2503.02059.

21. Zhang, C. et al. The composite spectrum of little red dots from a standard inner disk and an unstable outer disk. Nat. Astron. DOI: 10.1038/s41550-026-02785-x (2026). 2505.12719.

22. Zwick, L., Tiede, C. & Mayer, L. Little Red Dots as self-gravitating discs accreting on supermassive stars: Spectral appearance and formation pathway of the progenitors to direct collapse black holes. arXiv e-prints arXiv:2507.22014, DOI: 10.48550/arXiv.2507.22014 (2025). 2507.22014.

23. Chen, Y.-X. et al. Spectral Appearance of Self-gravitating AGN Disks Powered by Stellar Objects: Universal Effective Temperature in the Optical Continuum and Application to Little Red Dots. arXiv e-prints arXiv:2602.06954, DOI: 10.48550/arXiv.2602.06954 (2026). 2602.06954.

24. Kocevski, D. D. et al. The Rise of Faint, Red Active Galactic Nuclei at z > 4: A Sample of Little Red Dots in the JWST Extragalactic Legacy Fields. Astrophys. J. **986**, 126, DOI: 10.3847/1538-4357/adbc7d (2025). 2404.03576.

25. Tripodi, R. et al. Extreme properties of a compact and massive accreting black hole host in the first 500 Myr. Nat. Commun. **16**, 9830, DOI: 10.1038/s41467-025-65070-x (2025). 2412.04983.

26. Zhang, Y. et al. Unveiling Extended Components of 'Little Red Dots' in Rest-Frame Optical. arXiv e-prints arXiv:2510.25830, DOI: 10.48550/arXiv.2510.25830 (2025). 2510.25830.

27. Chen, C.-H., Ho, L. C., Li, R. & Zhuang, M.-Y. The Host Galaxy (If Any) of the Little Red Dots. Astrophys. J. **983**, 60, DOI: 10.3847/1538-4357/ada93a (2025). 2411.04446.

28. Juodžbalis, I. et al. A direct black hole mass measurement in a Little Red Dot at the Epoch of Reionization. arXiv e-prints arXiv:2508.21748, DOI: 10.48550/arXiv.2508.21748 (2025). 2508.21748.

29. Rusakov, V. et al. Little red dots as young supermassive black holes in dense ionized cocoons. Nature **649**, 574–579, DOI: 10.1038/s41586-025-09900-4 (2026). 2503.16595.

30. Ma, Y. et al. UNCOVER: 404 Error—Models Not Found for the Triply Imaged Little Red Dot A2744-QSO1. Astrophys. J. **981**, 191, DOI: 10.3847/1538-4357/ada613 (2025). 2410.06257.

31. Ji, X. et al. Lord of LRDs: insights into a 'Little Red Dot' with a low-ionization spectrum at z = 0.1. Mon. Not. R. Astron. Soc. **545**, staf2235, DOI: 10.1093/mnras/staf2235 (2026). 2507.23774.

32. Akins, H. B. et al. COSMOS-Web: The Overabundance and Physical Nature of "Little Red Dots"—Implications for Early Galaxy and SMBH Assembly. Astrophys. J. **991**, 37, DOI: 10.3847/1538-4357/ade984 (2025). 2406.10341.

33. McGreer, I. D. et al. The z = 5 quasar luminosity function from sdss stripe 82. Astrophys. J. **768**, 105, DOI: 10.1088/0004-637X/768/2/105 (2013). 1212.4493.

34. McGreer, I. D., Fan, X., Jiang, L. & Cai, Z. The Faint End of the z = 5 Quasar Luminosity Function from the CFHTLS. Astron. J. **155**, 131, DOI: 10.3847/1538-3881/aaaab4 (2018). 1710.09390.

35. Yang, J. et al. A Survey of Luminous High-redshift Quasars with SDSS and WISE. II. the Bright End of the Quasar Luminosity Function at z $\approx$ 5. Astrophys. J. **829**, 33, DOI: 10.3847/0004-637X/829/1/33 (2016). 1607.04415.

36. Jiang, L. et al. The Final SDSS High-redshift Quasar Sample of 52 Quasars at z>5.7. Astrophys. J. **833**, 222, DOI: 10.3847/1538-4357/833/2/222 (2016). 1610.05369.

37. Matsuoka, Y. et al. Subaru High-z Exploration of Low-luminosity Quasars (SHELLQs). X. Discovery of 35 Quasars and Luminous Galaxies at 5.7 $\leq$ z $\leq$ 7.0. Astrophys. J. **883**, 183, DOI: 10.3847/1538-4357/ab3c60 (2019). 1908.07910.

38. Schindler, J.-T. et al. The Pan-STARRS1 z > 5.6 Quasar Survey. III. The z $\approx$ 6 Quasar Luminosity Function. Astrophys. J. **943**, 67, DOI: 10.3847/1538-4357/aca7ca (2023). 2212.04179.

39. Wang, F. et al. Exploring Reionization-era Quasars. III. Discovery of 16 Quasars at 6.4 $\lesssim$ z $\lesssim$ 6.9 with DESI Legacy Imaging Surveys and the UKIRT Hemisphere Survey and Quasar Luminosity Function at z $\sim$ 6.7. Astrophys. J. **884**, 30, DOI: 10.3847/1538-4357/ab2be5 (2019). 1810.11926.

40. Matsuoka, Y. et al. Quasar Luminosity Function at z = 7. Astrophys. J. Lett. **949**, L42, DOI: 10.3847/2041-8213/acd69f (2023). 2305.11225.

41. Carranza-Escudero, M. et al. Lonely Little Red Dots: Challenges to the Active Galactic Nucleus Nature of Little Red Dots through Their Clustering and Spectral Energy Distributions. Astrophys. J. Lett. **989**, L50, DOI: 10.3847/2041-8213/adf73d (2025). 2506.04004.

42. Ma, Y. et al. Counting Little Red Dots at z < 4 with Ground-based Surveys and Spectroscopic Follow-up. Astrophys. J. **1000**, 59, DOI: 10.3847/1538-4357/ae4596 (2026). 2504.08032.

43. Inayoshi, K. Little Red Dots as the Very First Activity of Black Hole Growth. Astrophys. J. Lett. **988**, L22, DOI: 10.3847/2041-8213/adea66 (2025). 2503.05537.

44. Zhang, Z., Jiang, L., Liu, W., Ho, L. C. & Inayoshi, K. JWST Insights into Narrow-line Little Red Dots. Astrophys. J. **998**, 170, DOI: 10.3847/1538-4357/ae33c4 (2026). 2506.04350.

45. de Graaff, A. et al. Little Red Dots host Black Hole Stars: A unified family of gas-reddened AGN revealed by JWST/NIRSpec spectroscopy. arXiv e-prints arXiv:2511.21820, DOI: 10.48550/arXiv.2511.21820 (2025). 2511.21820.

46. Greene, J. E. & Ho, L. C. Estimating Black Hole Masses in Active Galaxies Using the Hα Emission Line. Astrophys. J. **630**, 122–129, DOI: 10.1086/431897 (2005). astro-ph/0508335.

47. Lin, X. et al. The Discovery of Little Red Dots in the Local Universe: Signatures of Cool Gas Envelopes. Astrophys. J. **997**, 364, DOI: 10.3847/1538-4357/ae2bdf (2026). 2507.10659.

48. Lin, X. et al. The Large-scale Environments of Low-luminosity AGNs at 3.9 < z < 6 and Implications for Their Host Dark Matter Halos from a Complete NIRCam Grism Redshift Survey. Astrophys. J. **997**, 61, DOI: 10.3847/1538-4357/ae1eef (2026). 2505.02896.

49. Davis, M., Efstathiou, G., Frenk, C. S. & White, S. D. M. The evolution of large-scale structure in a universe dominated by cold dark matter. Astrophys. J. **292**, 371–394, DOI: 10.1086/163168 (1985).

50. White, S. D. M. & Rees, M. J. Core condensation in heavy halos: a two-stage theory for galaxy formation and clustering. Mon. Not. R. Astron. Soc. **183**, 341–358, DOI: 10.1093/mnras/183.3.341 (1978).

51. Peebles, P. J. E. The large-scale structure of the universe (Princeton Univercity Press, 1980).

52. Shen, Y. et al. Clustering of High-Redshift (z >= 2.9) Quasars from the Sloan Digital Sky Survey. Astron. J. **133**, 2222–2241, DOI: 10.1086/513517 (2007). astro-ph/0702214.

53. Ross, N. P. et al. Clustering of Low-redshift (z <= 2.2) Quasars from the Sloan Digital Sky Survey. Astrophys. J. **697**, 1634–1655, DOI: 10.1088/0004-637X/697/2/1634 (2009). 0903.3230.

54. Eftekharzadeh, S. et al. Clustering of intermediate redshift quasars using the final SDSS III-BOSS sample. Mon. Not. R. Astron. Soc. **453**, 2779–2798, DOI: 10.1093/mnras/stv1763 (2015). 1507.08380.

55. Timlin, J. D. et al. The Clustering of High-redshift ($2.9 \leq z \leq 5.1$) Quasars in SDSS Stripe 82. Astrophys. J. **859**, 20, DOI: 10.3847/1538-4357/aab9ac (2018). 1712.03128.

56. He, W. et al. Clustering of quasars in a wide luminosity range at redshift 4 with Subaru Hyper Suprime-Cam Wide-field imaging. Publ. Astron. Soc. Jpn **70**, S33, DOI: 10.1093/pasj/psx129 (2018). 1704.08461.

57. Arita, J. et al. Subaru High-z Exploration of Low-luminosity Quasars (SHELLQs). XVIII. The Dark Matter Halo Mass of Quasars at z 6. Astrophys. J. **954**, 210, DOI: 10.3847/1538-4357/ace43a (2023). 2307.02531.

58. Eilers, A.-C. et al. EIGER. VI. The Correlation Function, Host Halo Mass, and Duty Cycle of Luminous Quasars at $z \gtrsim 6$. Astrophys. J. **974**, 275, DOI: 10.3847/1538-4357/ad778b (2024). 2403.07986.

59. Meng, H., Zhang, H. & Ye, G. Probing The Dark Matter Halo of High-redshift Quasar from Wide-Field Clustering Analysis. arXiv e-prints arXiv:2602.02778 (2026). 2602.02778.

60. Arita, J. et al. The nature of low-luminosity AGNs discovered by JWST based on clustering analysis: progenitors of low-z quasars? Mon. Not. R. Astron. Soc. **536**, 3677–3688, DOI: 10.1093/mnras/stae2765 (2025). 2410.08707.

61. Shuntov, M. et al. Constraints on the early Universe star formation efficiency from galaxy clustering and halo modeling of Hα and [O III] emitters. Astron. Astrophys. **699**, A231, DOI: 10.1051/0004-6361/202554618 (2025). 2503.14280.

62. Behroozi, P., Wechsler, R. H., Hearin, A. P. & Conroy, C. UNIVERSEMACHINE: The correlation between galaxy growth and dark matter halo assembly from z = 0-10. MNRAS **488**, 3143–3194, DOI: 10.1093/mnras/stz1182 (2019). 1806.07893.

63. Ferrarese, L. Beyond the Bulge: A Fundamental Relation between Supermassive Black Holes and Dark Matter Halos. Astrophys. J. **578**, 90–97, DOI: 10.1086/342308 (2002). astro-ph/0203469.

64. Robinson, J. H. et al. Tully-Fisher Distances and Dynamical Mass Constraints for 24 Host Galaxies of Reverberation-mapped AGNs. Astrophys. J. **912**, 160, DOI: 10.3847/1538-4357/abedaa (2021). 2103.07000.

65. Li, Q. et al. Black Hole–Halo Mass Relation from UNIONS Weak Lensing. Astrophys. J. Lett. **969**, L25, DOI: 10.3847/2041-8213/ad58b0 (2024). 2402.10740.

66. Zhuang, M.-Y. & Ho, L. C. Evolutionary paths of active galactic nuclei and their host galaxies. Nat. Astron. **7**, 1376–1389, DOI: 10.1038/s41550-023-02051-4 (2023). 2308.08603.

67. LaChance, P. et al. From ASTRID to BRAHMA – The role of overmassive black holes in little red dots in cosmological simulations. arXiv e-prints arXiv:2512.13957, DOI: 10.48550/arXiv.2512.13957 (2025). 2512.13957.

68. LaChance, P. et al. The Properties of Little Red Dot Galaxies in the ASTRID Simulation. The Open J. Astrophys. **9**, 55493, DOI: 10.33232/001c.155493 (2026). 2505.20439.

69. Pacucci, F. & Loeb, A. Cosmic Outliers: Low-spin Halos Explain the Abundance, Compactness, and Redshift Evolution of the Little Red Dots. Astrophys. J. Lett. **989**, L19, DOI: 10.3847/2041-8213/ade871 (2025). 2506.03244.

70. Sijacki, D., Springel, V. & Haehnelt, M. G. Growing the first bright quasars in cosmological simulations of structure formation. Mon. Not. R. Astron. Soc. **400**, 100–122, DOI: 10.1111/j.1365-2966.2009.15452.x (2009). 0905.1689.

71. Ward, E. et al. Evolution of the SizeMass Relation of Star-forming Galaxies Since z = 5.5 Revealed by CEERS. Astrophys. J. **962**, 176, DOI: 10.3847/1538-4357/ad20ed (2024). 2311.02162.

72. Yang, L. et al. COSMOS-Web: Unraveling the Evolution of Galaxy Size and Related Properties at 2 < z < 10. Astrophys. J. Suppl. Ser. **281**, 68, DOI: 10.3847/1538-4365/ae0e1b (2025). 2504.07185.

73. Jiang, F. et al. Formation of the Little Red Dots from the Core Collapse of Self-interacting Dark Matter Halos. Astrophys. J. Lett. **996**, L19, DOI: 10.3847/2041-8213/ae247a (2026). 2503.23710.

74. Bezanson, R. et al. The JWST UNCOVER Treasury Survey: Ultradeep NIRSpec and NIRCam Observations before the Epoch of Reionization. Astrophys. J. **974**, 92, DOI: 10.3847/1538-4357/ad66cf (2024). 2212.04026.

75. Finkelstein, S. L. et al. A Long Time Ago in a Galaxy Far, Far Away: A Candidate z $\sim$ 12 Galaxy in Early JWST CEERS Imaging. Astrophys. J. Lett. **940**, L55, DOI: 10.3847/2041-8213/ac966e (2022). 2207.12474.

76. Eisenstein, D. J. et al. Overview of the JWST Advanced Deep Extragalactic Survey (JADES). arXiv e-prints arXiv:2306.02465, DOI: 10.48550/arXiv.2306.02465 (2023). 2306.02465.

77. Dunlop, J. S. et al. PRIMER: Public Release IMaging for Extragalactic Research. JWST Proposal. Cycle 1, ID. #1837 (2021).

78. Valentino, F. et al. An Atlas of Color-selected Quiescent Galaxies at z > 3 in Public JWST Fields. Astrophys. J. **947**, 20, DOI: 10.3847/1538-4357/acbefa (2023). 2302.10936.

79. Brammer, G. grizli (2023). Zenodo identifier: 8370018.

80. Brammer, G. msaexp: Nirspec analysis tools (2023). Zenodo identifier: 8319596.

81. Brammer, G. B., van Dokkum, P. G. & Coppi, P. EAZY: A Fast, Public Photometric Redshift Code. Astrophys. J. **686**, 1503–1513, DOI: 10.1086/591786 (2008). 0807.1533.

82. Furtak, L. J. et al. UNCOVERing the extended strong lensing structures of Abell 2744 with the deepest JWST imaging. Mon. Not. R. Astron. Soc. **523**, 4568–4582, DOI: 10.1093/mnras/stad1627 (2023). 2212.04381.

83. Price, S. H. et al. The UNCOVER Survey: First Release of Ultradeep JWST/NIRSpec PRISM Spectra for ∼700 Galaxies from z ∼ 0.313 in A2744. Astrophys. J. **982**, 51, DOI: 10.3847/1538-4357/adaec1 (2025). 2408.03920.

84. Ye, G., Zhang, H. & Wu, Q. Machine Learning–based Search of High-redshift Quasars. Astrophys. J. Suppl. Ser. **275**, 19, DOI: 10.3847/1538-4365/ad79ee (2024). 2409.02167.

85. Merlin, E. et al. ASTRODEEP-JWST: NIRCam-HST multi-band photometry and redshifts for half a million sources in six extragalactic deep fields. Astron. Astrophys. **691**, A240, DOI: 10.1051/0004-6361/202451409 (2024). 2409.00169.

86. DESI Collaboration et al. The DESI Experiment Part I: Science,Targeting, and Survey Design. arXiv e-prints arXiv:1611.00036 (2016). 1611.00036.

87. DESI Collaboration et al. The DESI Experiment Part II: Instrument Design. arXiv e-prints arXiv:1611.00037 (2016). 1611.00037.

88. DESI Collaboration et al. Data Release 1 of the Dark Energy Spectroscopic Instrument. Astron. J. **171**, 285, DOI: 10.3847/1538-3881/ae4c43 (2026). 2503.14745.

89. Ross, A. J. et al. The construction of large-scale structure catalogs for the Dark Energy Spectroscopic Instrument. J. Cosmol. Astropart. Phys. **2025**, 125, DOI: 10.1088/1475-7516/2025/01/125 (2025). 2405.16593.

90. Adame, A. G. et al. DESI 2024 II: sample definitions, characteristics, and two-point clustering statistics. J. Cosmol. Astropart. Phys. **2025**, 017, DOI: 10.1088/1475-7516/2025/07/017 (2025). 2411.12020.

91. Dey, A. et al. Overview of the DESI Legacy Imaging Surveys. Astron. J. **157**, 168, DOI: 10.3847/1538-3881/ab089d (2019). 1804.08657.

92. Zhou, R. et al. DESI luminous red galaxy samples for cross-correlations. J. Cosmol. Astropart. Phys. **2023**, 097, DOI: 10.1088/1475-7516/2023/11/097 (2023). 2309.06443.

93. Zhou, R. et al. The clustering of DESI-like luminous red galaxies using photometric redshifts. Mon. Not. R. Astron. Soc. **501**, 3309–3331, DOI: 10.1093/mnras/staa3764 (2021). 2001.06018.

94. Landy, S. D. & Szalay, A. S. Bias and Variance of Angular Correlation Functions. Astrophys. J. **412**, 64, DOI: 10.1086/172900 (1993).

95. Davis, M. & Peebles, P. J. E. A survey of galaxy redshifts. V. The two-point position and velocity correlations. Astrophys. J. **267**, 465–482, DOI: 10.1086/160884 (1983).

96. Murray, S. G., Power, C. & Robotham, A. S. G. HMFcalc: An online tool for calculating dark matter halo mass functions. Astron. Comput. **3**, 23, DOI: 10.1016/j.ascom.2013.11.001 (2013). 1306.6721.

97. Murray, S. G. et al. THEHALOMOD: An online calculator for the halo model. Astron. Comput. **36**, 100487, DOI: 10.1016/j.ascom.2021.100487 (2021). 2009.14066.

98. Tinker, J. L. et al. The Large-scale Bias of Dark Matter Halos: Numerical Calibration and Model Tests. Astrophys. J. **724**, 878–886, DOI: 10.1088/0004-637X/724/2/878 (2010). 1001.3162.

99. Lewis, A., Challinor, A. & Lasenby, A. Efficient Computation of Cosmic Microwave Background Anisotropies in Closed Friedmann-Robertson-Walker Models. Astrophys. J. **538**, 473–476, DOI: 10.1086/309179 (2000). astro-ph/9911177.

100. Carroll, S. M. The Cosmological Constant. Living Rev. Relativ. **4**, 1, DOI: 10.12942/lrr-2001-1 (2001). astro-ph/0004075.

101. Mountrichas, G. et al. QSO-LRG two-point cross-correlation function and redshift-space distortions. Mon. Not. R. Astron. Soc. **394**, 2050–2064, DOI: 10.1111/j.1365-2966.2009.14456.x (2009). 0801.1816.

102. Behroozi, P. S., Wechsler, R. H. & Conroy, C. The Average Star Formation Histories of Galaxies in Dark Matter Halos from z = 0-8. Astrophys. J. **770**, 57, DOI: 10.1088/0004-637X/770/1/57 (2013). 1207.6105.

103. Shuntov, M. et al. COSMOS2020: Cosmic evolution of the stellar-to-halo mass relation for central and satellite galaxies up to z $\sim$ 5. Astron. Astrophys. **664**, A61, DOI: 10.1051/0004-6361/202243136 (2022). 2203.10895.

104. Shuntov, M. et al. COSMOS-Web: Stellar mass assembly in relation to dark matter halos across 0.2 < z < 12 of cosmic history. Astron. Astrophys. **695**, A20, DOI: 10.1051/0004-6361/202452570 (2025). 2410.08290.